NEATH – II. N_2H^+ as a tracer of imminent star formation in quiescent high-density gas

F. D. Priestley,[1]⋆ P. C. Clark [ORCID],[1] S. C. O. Glover [ORCID],[2] S. E. Ragan [ORCID],[1] O. Fehér,[1] L. R. Prole[3] and R. S. Klessen [ORCID][2,4]

[1] *School of Physics and Astronomy, Cardiff University, Queen's Buildings, The Parade, Cardiff CF24 3AA, UK*
[2] *Institut für Theoretische Astrophysik, Zentrum für Astronomie, Universität Heidelberg, Albert-Ueberle-Straße 2, D-69120 Heidelberg, Germany*
[3] *Centre for Astrophysics and Space Science Maynooth, Department of Theoretical Physics, Maynooth University, Maynooth W23 F2H6, Ireland*
[4] *Interdisziplinäres Zentrum für Wissenschaftliches Rechnen, Universität Heidelberg, Im Neuenheimer Feld 205, D-69120 Heidelberg, Germany*

ABSTRACT

Star formation activity in molecular clouds is often found to be correlated with the amount of material above a column density threshold of $\sim 10^{22}$ cm^{-2}. Attempts to connect this column density threshold to a *volume* density above which star formation can occur are limited by the fact that the volume density of gas is difficult to reliably measure from observations. We post-process hydrodynamical simulations of molecular clouds with a time-dependent chemical network, and investigate the connection between commonly observed molecular species and star formation activity. We find that many molecules widely assumed to specifically trace the dense, star-forming component of molecular clouds (e.g. HCN, HCO$^+$, CS) actually also exist in substantial quantities in material only transiently enhanced in density, which will eventually return to a more diffuse state without forming any stars. By contrast, N_2H^+ only exists in detectable quantities above a volume density of 10^4 cm^{-3}, the point at which CO, which reacts destructively with N_2H^+, begins to deplete out of the gas phase on to grain surfaces. This density threshold for detectable quantities of N_2H^+ corresponds very closely to the volume density at which gas becomes irreversibly gravitationally bound in the simulations: the material traced by N_2H^+ never reverts to lower densities, and quiescent regions of molecular clouds with visible N_2H^+ emission are destined to eventually form stars. The N_2H^+ line intensity is likely to directly correlate with the star formation rate averaged over time-scales of around a Myr.

Key words: astrochemistry – stars: formation – ISM: clouds – ISM: molecules.

1 INTRODUCTION

Stars form in molecular clouds, specifically in the densest regions (often referred to as cores or clumps; Bergin & Tafalla 2007) where self-gravity is able to overcome the various forces opposing collapse. Lada, Lombardi & Alves (2010) proposed that star formation *only* occurs in regions with *K*-band extinctions $A_K \gtrsim 0.8$ mag, based on the correlation between the mass of material above this threshold and the star formation rate (as traced by the number of protostars in the cloud). Studies using entirely independent methods (e.g. Könyves et al. 2015) have found evidence of similar thresholds for star formation activity, corresponding to a visual extinction of $A_V \sim 8$ mag or a column density of $N_H \sim 10^{22}$ cm^{-2}, but the significance of this value and the reasons for its existence remain unclear.

One limitation of observational studies is that they are restricted to probing the line-of-sight column density, while the *volume* density of the gas is presumably more relevant to its evolution; the Jeans mass, for example, scales with local gas properties ($M_J \propto \rho^{-1/2} T^{3/2}$;

Klessen & Glover 2016) rather than the column of material. Lada, Lombardi & Alves (2010) argue that their column density threshold corresponds to a volume density of $n_H \sim 10^4$ cm^{-3}, but this relies on the assumption of a specific cloud geometry, and in reality one would expect a distribution of volume densities along the line of sight, rather than a single value. Establishing line-of-sight structure in molecular clouds is fraught with difficulties; see, for example, the ongoing debate about whether the Musca cloud is a filament or an edge-on sheet (Tritsis et al. 2022; Kaminsky et al. 2023).

A common approach to mitigate this issue is to assume that the high volume density gas associated with star formation is specifically traced by molecular lines with high critical densities, most commonly the $J = 1$–0 HCN transition. However, the emission in these lines is typically dominated by material with significantly lower density ($\sim 10^3$ cm^{-3}; Kauffmann et al. 2017; Pety et al. 2017; Evans et al. 2020; Jones et al. 2023; Neumann et al. 2023) than the assumed threshold for star formation, making them unsuitable for this purpose. The one exception appears to be the N_2H^+ $J = 1$–0 line, which is almost exclusively detected in regions with column densities above 10^{22} cm^{-2} (Kauffmann et al. 2017; Tafalla, Usero & Hacar 2021), coinciding quite closely with the Lada, Lombardi & Alves (2010) column density threshold for star formation.

⋆ E-mail: priestleyf@cardiff.ac.uk

Table 1. Simulation collision velocities, total durations, durations of star formation (time after formation of the first sink particle), final mass ($M_{\rm sink}$) and number ($N_{\rm sink}$) of sink particles, the final mass of gas with density above 10^3 cm^{-3} ($M_{\rm mid}$) and 10^4 cm^{-3} ($M_{\rm dense}$), and the average star formation rate (defined as $M_{\rm sink}/t_{\rm SF}$).

Model	$v_{\rm col}$ (km s^{-1})	$t_{\rm end}$ (Myr)	$t_{\rm SF}$ (Myr)	$M_{\rm sink}$ (M$_\odot$)	$N_{\rm sink}$	$M_{\rm mid}$ (M$_\odot$)	$M_{\rm dense}$ (M$_\odot$)	$\langle {\rm SFR} \rangle$ (M$_\odot$ Myr^{-1})
V3	3	6.79	1.22	155	86	3341	263	127
V7	7	5.53	1.70	102	105	2986	211	60
V10	10	7.66	1.13	74	35	1610	265	65
V14	14	8.70	–	0	0	4	0	–

Another limitation is that observations can only capture a single moment of a molecular cloud's Myr-scale lifetime. While previous levels of star formation activity can be measured, such as by counting the number of protostellar objects as in Lada, Lombardi & Alves (2010), the potential of a cloud for future star formation is not easily accessible. Many studies divide objects between those that are gravitationally bound, and so presumably destined to collapse, and unbound (and therefore transient) objects, but this distinction relies on a number of quantities that are either difficult or impossible to measure accurately (Enoch et al. 2008), and neglects the possibility of continuing accretion of material (Anderson et al. 2021; Rigby et al. 2021).

In this paper, we post-process hydrodynamical simulations of molecular clouds with a time-dependent chemical network, and investigate molecular tracers of material that *will* form stars. We find that N$_2$H$^+$ only exists in substantial quantities in gas that is irreversibly undergoing gravitational collapse, making it a unique signature of future star formation activity in molecular clouds.

2 METHOD

We perform simulations of colliding, initially atomic clouds using AREPO (Springel 2010), a moving-mesh magnetohydrodynamic code. The simulations include an extensive suite of processes affecting the thermodynamics of the gas and dust (Glover & Mac Low 2007; Glover & Clark 2012), including an on-the-fly chemical network [a modified version of the Gong, Ostriker & Wolfire (2017) network, as described in Hunter et al. (2023)] for the key atomic and molecular coolants, with self-shielding from the external ultraviolet (UV) radiation field calculated self-consistently (Clark, Glover & Klessen 2012).

We initialize two spherical clouds of mass 10^4 M$_\odot$ and radius 19 pc, for an initial volume density of 10 cm^{-3} and a gas (dust) temperature of 300 K (15 K), displaced along the x-axis so that the clouds are initially just touching. The clouds have a virialized turbulent velocity field with a root-mean-square value of 0.95 km s^{-1}, and a bulk motion along the x-axis $v_x = \pm v_{\rm col}$ for the cloud displaced in the $\mp x$ direction; we investigate four values of $v_{\rm col}$ between 3 and 14 km s^{-1}, giving net collision velocities $2v_{\rm col}$ between 6 and 28 km s^{-1}. Model properties are listed in Table 1. A 3 μG magnetic field is included parallel to the collision axis. Sink particles are introduced following Tress et al. (2020) (see also Prole et al. 2022), with a threshold density of 2×10^{-16} g cm^{-3} and formation radius of 9×10^{-4} pc.

We use Monte Carlo tracer particles (Genel et al. 2013) to record the evolution of the physical properties of individual parcels of gas. We then post-process the time-dependent chemical evolution of the tracers with the NEATH framework[1] (Priestley et al. 2023), using a

[1] https://fpriestley.github.io/neath/

Table 2. Elemental abundances used in the chemical modelling.

Element	Abundance	Element	Abundance
C	1.4×10^{-4}	S	1.2×10^{-5}
N	7.6×10^{-5}	Si	1.5×10^{-7}
O	3.2×10^{-4}	Mg	1.4×10^{-7}

modified version of the UCLCHEM code (Holdship et al. 2017) with the UMIST12 reaction network (McElroy et al. 2013). We assume elemental abundances from Sembach et al. (2000) with the refractory elements depleted by an additional factor of 100 (as is appropriate for the dense interstellar medium; Lee et al. 1998; Jenkins 2009), listed in Table 2. The external UV field is set to 1.7 Habing units (Habing 1968) and the cosmic ray ionization rate to 10^{-16} s^{-1}. These chemical parameters are shared with the underlying AREPO simulations.

We select 10^5 tracer particles from each simulation to model chemically, chosen from particles with a final position within 16.2 pc of the simulation centre; this region includes virtually all of the dense gas in the simulations. Particles are chosen to evenly sample final densities in the range $10–10^6$ cm^{-3}, with the exception of the V14 simulation, where the upper boundary is the maximum density present at the simulation end point (2000 cm^{-3}). The limit of 10^6 cm^{-3} is motivated by the 44 kyr time resolution of the simulations (i.e. the interval between updates of tracer properties), which is insufficient to fully resolve the freefall time of gas at higher densities. This leads to the rapidly evolving physical properties in collapsing regions not being captured by the chemical modelling, making the resulting molecular abundances unreliable. A time resolution of 44 kyr produces abundances that are converged up to gas densities of 10^5 cm^{-3}, and accurate to within a factor of 2 up to 10^6 cm^{-3} (Priestley et al. 2023), which is more than sufficient for our purposes.

3 RESULTS

3.1 Physical properties

Table 1 lists the mass and number of sinks formed in each of the four simulations, and the mass of gas above volume density thresholds of 10^3 and 10^4 cm^{-3} at the final time $t_{\rm end}$. We choose $t_{\rm end}$ so that the V3, V7, and V10 simulations have all formed a similar quantity of dense ($n_{\rm H} > 10^4$ cm^{-3}) gas; the V14 simulation is evolved to the point where it appears to be dispersing, as it never forms any substantial amount of dense gas.

Fig. 1 shows the simulation column densities, viewed perpendicular to the collision axis at $t_{\rm end}$. The V3 and V7 models have both formed a compressed layer at the interface between the two clouds, which contains the vast majority of the dense material. In the V10 simulation, the higher kinetic energy of the initial cloud motions has disrupted this layer, and the dense material is more spread
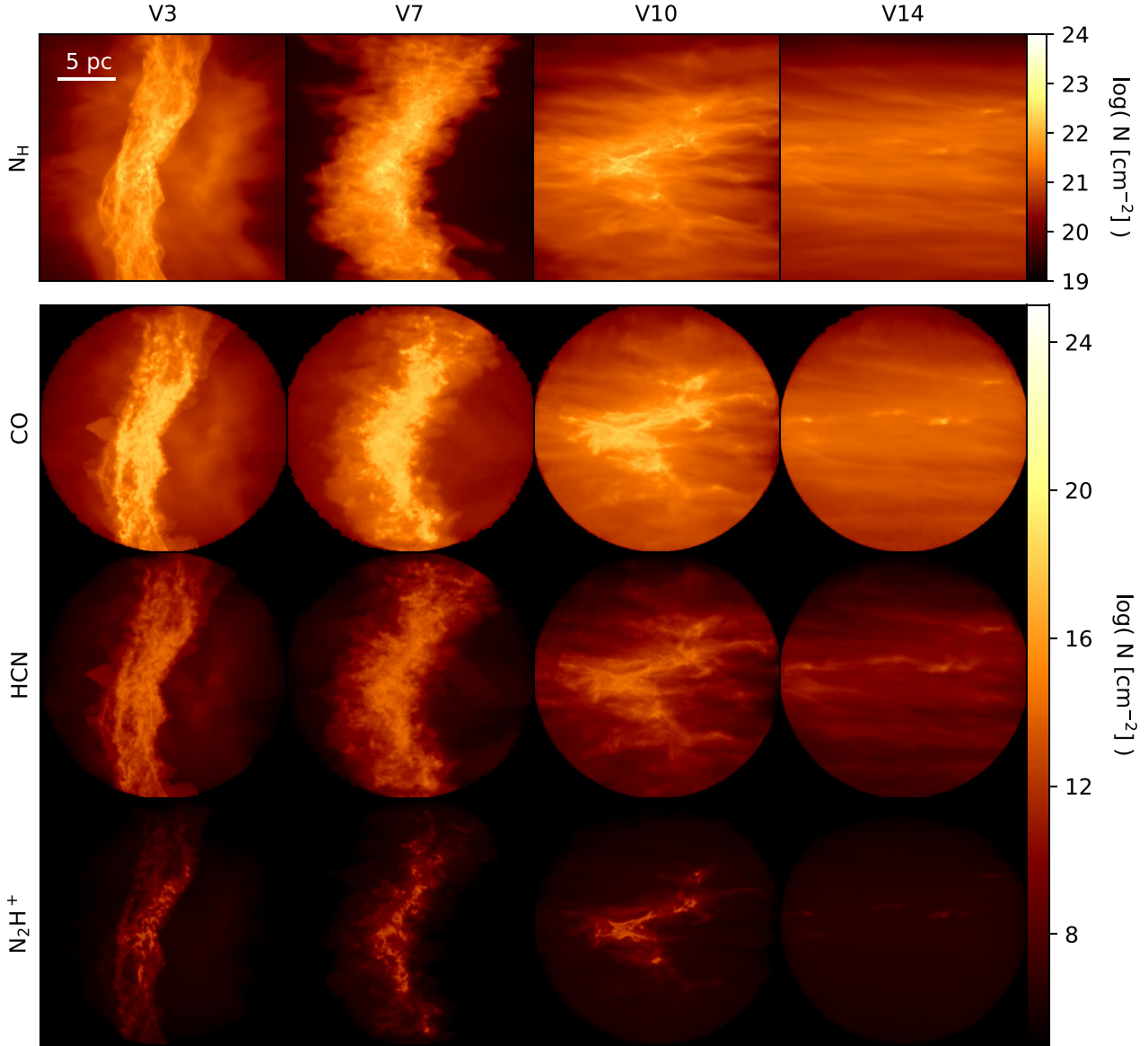
Figure 1. Column densities of hydrogen nuclei (top row), CO (second row), HCN (third row), and N_2H^+ (bottom row) for the four simulations. The initial bulk velocities of the clouds are oriented along the horizontal axis. Note that all post-processed tracer particles are located within a sphere of radius 16.2 pc, so the molecular column densities outside the projected boundaries of this sphere are set to zero.

out along the collision axis. In the V14 simulation, the collision velocity is so high that no layer forms, and there is very little visible dense substructure. Some of the overdense regions that do form may eventually collapse under their own self-gravity (as in Jones et al. 2023), but there is no sign of this happening at the point we terminate the simulation.

Fig. 2 shows the time evolution of the masses of intermediate density (M_{mid}; $n_H > 10^3$ cm^{-3}) and genuinely dense gas (M_{dense}, defined using a volume density threshold of 10^4 cm^{-3} as suggested by Lada, Lombardi & Alves 2010), and the total mass accreted on to sink particles (M_{sink}). Intermediate-density gas forms earlier for faster collision velocities, but the two higher velocity models subsequently show a decline in the mass of this material, which for the V14 model appears to be irreversible. The onset of dense gas and sink formation has a more complex relationship with v_{col};

model V7 forms dense gas and sinks before V3, but has a slower rate of star formation, as indicated by the lower average values[2] in Table 1. Model V10 first forms dense gas at a comparable time to V7, but this gas then disperses before a second round of dense gas formation several Myr later, this time accompanied by sink formation. Model V14 never forms any significant quantity of dense gas, nor any sinks, over the runtime of the simulation. Star formation activity (as represented by sink particles) only seems to occur after the formation of a substantial ($>10\,M_\odot$) mass of dense gas. The mass of stars formed approximately tracks the mass of this dense gas with a delay of $\sim$1–2 Myr.

---

[2]We note that the star formation rates in our simulations are comparable to those estimated observationally by Lada, Lombardi & Alves (2010).
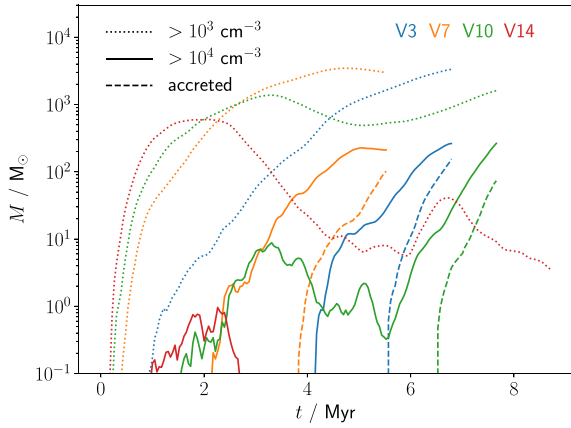
Figure 2. Time evolution of the mass of intermediate ($n_H > 10^3$ cm^{-3}; dotted lines) and high ($n_H > 10^4$ cm^{-3}; solid lines) density gas, and accreted sink mass (dashed lines), for the four simulations.

3.2 Chemical properties

Fig. 1 shows the column densities of CO, which is typically thought to trace gas with densities above ~ 100 cm^{-3} (e.g. Clark et al. 2019), and HCN and N_2H^+, both commonly used as tracers of denser gas. Regions of significant CO column density exist above a threshold total column of $\sim 10^{21}$ cm^{-2} (Priestley et al. 2023), but much of the substructure in regions above this threshold is not visible in the CO column; there is essentially no distinction between moderate- and high-density sightlines. HCN fares slightly better, but substantial columns are still present in fairly low-density sightlines, in agreement with its widespread detection in regions of molecular clouds with $A_V < 8$ mag (e.g. Evans et al. 2020).

As found by previous observational studies (Kauffmann et al. 2017; Tafalla, Usero & Hacar 2021), N_2H^+ only exists in significant quantities for $N_H \gtrsim 10^{22}$ cm^{-2} (Priestley et al. 2023). This is apparent in Fig. 1, where the morphology of the clouds seen in N_2H^+ is very different to that in CO or HCN, with only the highest density substructures being visible. The V14 model, which forms no sink particles, also has no substantial N_2H^+ column density along any sightline. This suggests a possible role for the molecule as a direct tracer of material with the potential to form stars.

Fig. 3 shows the distribution of tracer particles[3] in the post-processed sample, according to the peak density reached at any point during their evolution, and the final density at t_{end}, for the V7 model (the intermediate case out of the three models that form sink particles). Tracer particles that fall below the one-to-one relationship (represented by the dashed black line) were, at some point, at a higher density than their final value; they have undergone a transient enhancement in density, which has not resulted in runaway gravitational collapse.

Up to a peak density of about 10^4 cm^{-3}, there is a significant population of tracers below the one-to-one line. These tracers reached relatively high densities due to compression by supersonic gas motions, but subsequently returned to much lower values,[4] extending

---

[3] As the tracer particles do not correspond to physical gas parcels, this is not a direct measure of the mass distribution, but is a reasonable proxy quantity.
[4] This re-expansion is also due to the turbulent gas motions, as the magnetic field strength is – by design – too weak to prevent the collapse of gravitationally bound structures.
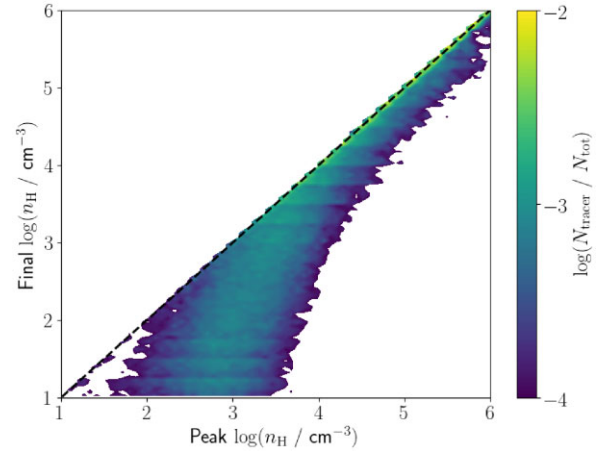
Figure 3. Distribution of tracer particles by peak density reached during the duration of the simulation, and the density at the simulation end, for the V7 model. The dashed black line shows the one-to-one relationship for tracer particles that only reach their peak density at the end of the simulation.

down to the initial cloud density of 10 cm^{-3}. By contrast, this behaviour is almost non-existent above a peak density of 10^4 cm^{-3}. Material that reaches this density never becomes strongly rarefied in its subsequent evolution, and is effectively destined to form (or accrete on to) a sink particle. This corresponds very well with the volume density threshold proposed by Lada, Lombardi & Alves (2010), and appears to be a natural outcome of the combined hydrodynamical and thermal evolution of molecular gas, although the exact reasons for the existence and value of this threshold are currently unclear.

Fig. 4 shows how the peak molecular abundances of CO, HCN, and N_2H^+ vary with the peak and final densities reached by the tracer particles, again for the V7 model. In addition to their limited ability to discern high-density substructures, CO and HCN both reach high peak abundances (relative to their maximum gas-phase abundance at any density) in material that reaches densities of a few thousand cm^{-3}, but subsequently returns to ~ 10 cm^{-3} and thus plays no role in star formation. By contrast, N_2H^+ has an abundance of $\lesssim 10^{-12}$ in this material, which we demonstrate in Section 3.4 would be observationally challenging to detect. Significant quantities of this molecule are only produced in gas that reaches, and then stays above, the 10^4 cm^{-3} density threshold.

Figs 5 and 6 show that this behaviour – for both the physical and chemical evolution – is independent of the simulation collision velocity. For all models, we find substantial quantities of gas that reaches a density above 10^3 cm^{-3} and subsequently returns to much lower values, but this behaviour is vanishingly rare for material that exceeds a volume density of 10^4 cm^{-3}. This volume density threshold for eventual gravitational collapse corresponds very closely to the density at which significant quantities of N_2H^+ are produced. We therefore suggest that detectable N_2H^+ emission in a molecular cloud directly traces material that is destined to eventually form stars, rather than transiently enhanced, unbound material, which may eventually disperse.

This behaviour is not shared by any other molecular species we investigate. Fig. 7 shows the behaviour of NH_3, HCO^+, and CS for the V7 model, all of which are often assumed to trace high-density, star-forming material. While NH_3 and HCO^+ reach their peak abundances only in material that exceeds the 10^4 cm^{-3} threshold for subsequent collapse, both molecules also exist in appreciable quantities below this boundary. CS behaves more like HCN and CO, and is even more
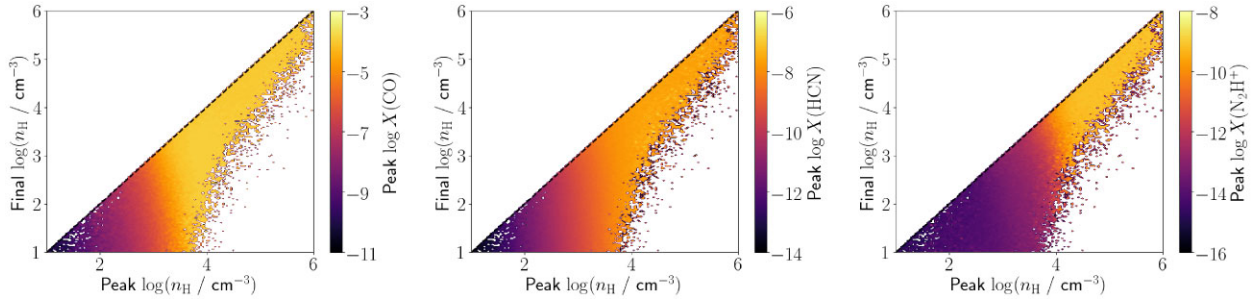
Figure 4. Average peak gas-phase abundances of CO (left), HCN (centre), and N$_2$H$^+$ (right), as a function of the peak density reached during the duration of the simulation, and the density at the simulation end, for the V7 model. The dashed black lines show the one-to-one relationship for tracer particles that only reach their peak density at the end of the simulation.
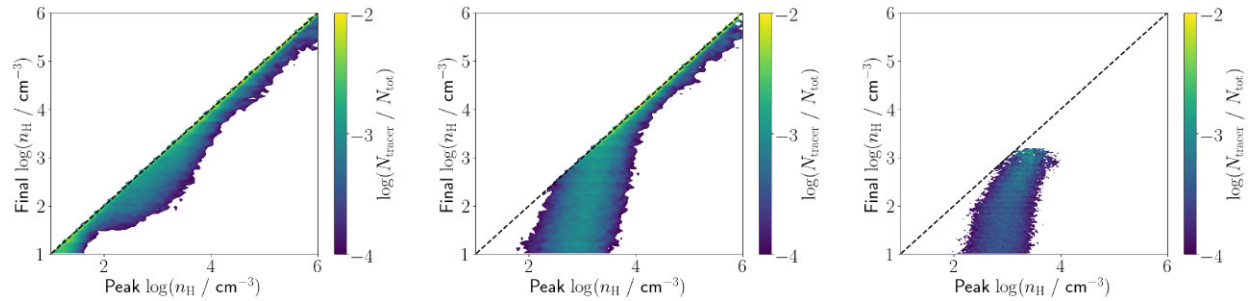
Figure 5. Distribution of tracer particles by peak density reached during the duration of the simulation, and the density at the simulation end, for the V3 (left), V10 (centre), and V14 (right) models. The dashed black lines show the one-to-one relationship for tracer particles that only reach their peak density at the end of the simulation.
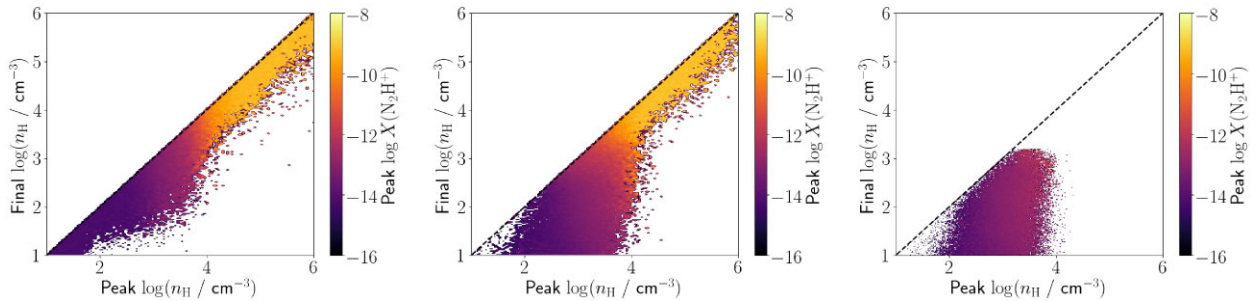
Figure 6. Average peak gas-phase abundances of N$_2$H$^+$ as a function of the peak density reached during the duration of the simulation, and the density at the simulation end, for the V3 (left), V10 (centre), and V14 (right) models. The dashed black lines show the one-to-one relationship for tracer particles that only reach their peak density at the end of the simulation.
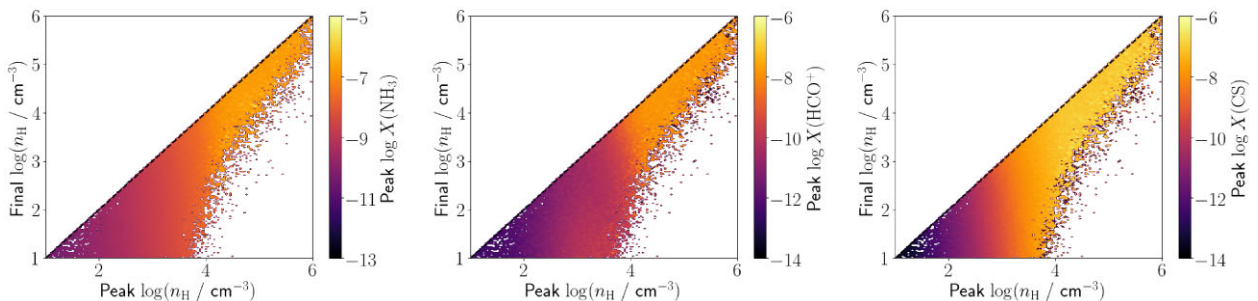
Figure 7. Average peak gas-phase abundances of NH$_3$ (left), HCO$^+$ (centre), and CS (right), as a function of the peak density reached during the duration of the simulation, and the density at the simulation end, for the V7 model. The dashed black lines show the one-to-one relationship for tracer particles that only reach their peak density at the end of the simulation.
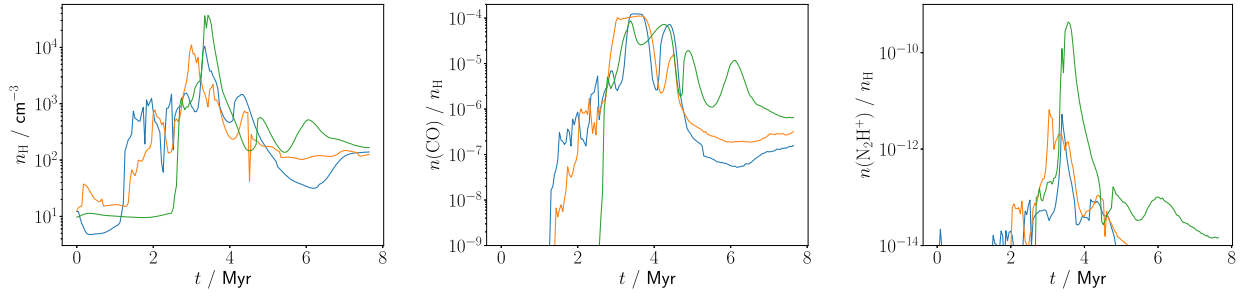
Figure 8. Evolution of the gas density (left) and the CO (centre) and N_2H^+ (right) abundances, for three tracer particles with peak density $>10^4 \, cm^{-3}$ and final density $<10^3 \, cm^{-3}$ from the V10 model.

likely to be readily detectable in material that is only transiently enhanced in density. We address the detectability issue quantitatively in Section 3.4 below.

3.3 Transient high-density gas

The two faster collisions, models V10 and V14, do appear to produce some dense gas that is not directly associated with star formation, reflected in the temporary peaks in dense gas mass between $\sim$2 and 3 Myr in Fig. 2. Fig. 8 shows the time evolution of three tracer particles from the V10 model, which have peak densities above $10^4 \, cm^{-3}$ but final densities significantly below this. The enhancement to high density is extremely brief ($\ll$Myr) in all cases, and the tracer particles quickly return to lower densities of $\sim$100 cm^{-3}.

The increase in density initially results in a rapid increase in the abundances of both CO and N_2H^+. However, once the CO abundance reaches $\sim$10^{-5}, its ability to efficiently destroy N_2H^+ terminates the rise in the abundance of the latter species, and two of the three tracer particles never exceed an N_2H^+ abundance of 10^{-11}. One tracer particle does reach a high enough density to begin depleting CO from the gas phase, allowing a peak N_2H^+ abundance of 10^{-10} that we show in Section 3.4 may be observationally relevant, but this only lasts for the brief period of time when the gas is at high density. Once the density begins to decline again, CO is rapidly desorbed back off grain surfaces, as the rates of the main desorption processes (via cosmic rays and UV photons) decline more slowly (proportional to n_H) than freeze-out (proportional to n_H^2). This causes a steep reduction in the abundance of N_2H^+.

Forming and maintaining a high N_2H^+ abundance requires depletion of CO, which itself requires high densities. The rate of depletion on to grain surfaces is given by

$$\dot{n}_{freeze} = 4.57 \times 10^4 \, \langle d_g a^2 \rangle \, (T/m)^{0.5} \, n_H \, n \quad cm^{-3} \, s^{-1}, \qquad (1)$$

where n is the gas-phase abundance of the molecule, $\pi \langle d_g a^2 \rangle$ is the grain surface area per hydrogen nucleus, T is the gas temperature, m is the atomic mass of the molecule, and we have assumed a sticking coefficient of unity (Rawlings et al. 1992). Taking $n_H = 10^4 \, cm^{-3}$, $T = 20$ K, $m = 28$ for CO, and $\langle d_g a^2 \rangle = 2.2 \times 10^{-22} \, cm^2$ from Rawlings et al. (1992), the freeze-out time-scale is $t_{freeze} = n/\dot{n}_{freeze} = 0.34$ Myr. In Fig. 9, we compare this value with the amount of time spent by tracer particles above a density of $10^4 \, cm^{-3}$, t_{dense} (CO freeze-out is inefficient at lower densities; Priestley et al. 2023), for the V10 model (we exclude tracer particles for which $t_{dense} = 0$). Virtually all tracer particles with a final density below $10^4 \, cm^{-3}$ have $t_{dense} < t_{freeze}$; material that reaches high densities only transiently does not spend enough time under these conditions to deplete CO, and
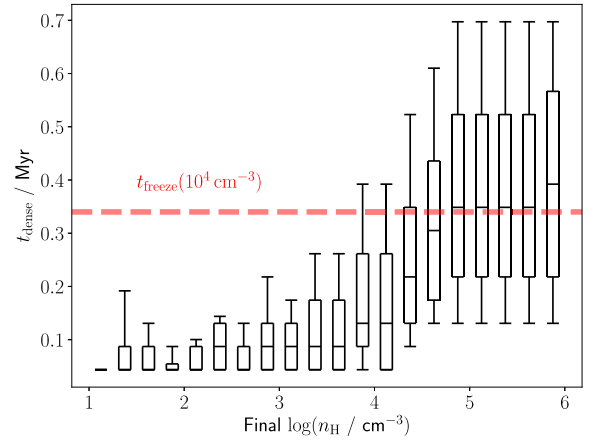
Figure 9. Distribution of time spent above $10^4 \, cm^{-3}$ (t_{dense}) versus final density, for all tracer particles with a peak density above $10^4 \, cm^{-3}$ in the V10 model. Boxes show the median and 25th/75th percentiles and whiskers the 10th and 90th percentiles. The dashed red line shows the freeze-out time-scale at a density of $10^4 \, cm^{-3}$ (0.34 Myr).

so does not form significant quantities of N_2H^+. For final densities above $10^4 \, cm^{-3}$, $t_{dense} \sim t_{freeze}$, and CO is sufficiently depleted for substantial quantities of N_2H^+ to survive. As t_{freeze} scales as n_H^{-1}, even tracer particles with $t_{dense} < 0.34$ Myr can deplete most of their CO if their final density is above $10^4 \, cm^{-3}$, as they only need to spend a small fraction of time at the higher density in order for freeze-out to proceed to completion.

3.4 Detectability of line emission

We estimate the intensity of molecular emission lines as a function of volume density using RADEX (van der Tak et al. 2007), assuming a uniform slab geometry. The required input parameters are the volume density and temperature of the gas, the column density of the molecule in question, and the velocity dispersion in the slab. Both the gas temperature and the total column density are quite tightly correlated with volume density in our simulations, so we adopt the power-law fits to the average relationships between these quantities from Priestley et al. (2023) to obtain temperature and total column[5] as

---

[5]Strictly speaking, this is the effective shielding column, not the line-of-sight value required by the radiative transfer model. However, the difference between these two quantities is typically small enough to make no qualitative difference to our results (Clark & Glover 2014).

Table 3. Input parameters used for the radiative transfer modelling.

n_H (cm^{-3})	T (K)	N_H (cm^{-2})	σ_v (km s^{-1})	$X(N_2H^+)$	$X(HCO^+)$	$X(HCN)$	$X(CS)$	$X(NH_3)$
10^2	47	1.2×10^{21}	1.0	10^{-14}	10^{-12}	10^{-12}	10^{-12}	10^{-10}
10^3	23	2.4×10^{21}	1.0	10^{-13}	10^{-10}	10^{-9}	10^{-9}	10^{-8}
10^4	15	4.8×10^{21}	1.0	10^{-11}	10^{-9}	10^{-8}	10^{-8}	10^{-7}
10^5	10	9.5×10^{21}	1.0	10^{-10}	10^{-8}	10^{-8}	10^{-7}	10^{-6}
10^6	7	1.9×10^{22}	1.0	10^{-10}	10^{-8}	10^{-8}	10^{-7}	10^{-6}
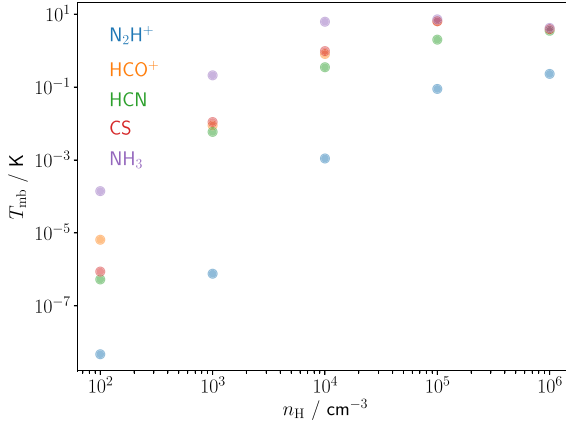
Figure 10. Main beam temperature versus density for the $J = 1$–0 lines of N_2H^+ (blue), HCO^+ (orange), and HCN (green), the $J = 2$–1 line of CS (red), and the $(1, 1)$ inversion transition of NH_3 (purple).

a function of density. We then convert the total column to the column density of the relevant molecule using its typical abundance in gas of the required volume density, estimated from Figs 4 and 7. As there is no equivalent relationship between velocity dispersion and gas density, we assume a value of $1.0\,\mathrm{km\,s^{-1}}$ typical of molecular clouds, and note that observed line widths do not appear to vary strongly with density (Tafalla, Usero & Hacar 2021). Input parameters used in the modelling are given in Table 3.

Fig. 10 shows the main beam temperatures as a function of density for the $J = 1$–0 lines of N_2H^+, HCO^+, and HCN, and the $J = 2$–1 CS line, all of which are commonly observed in 3 mm line surveys (e.g. Kauffmann et al. 2017; Pety et al. 2017; Tafalla, Usero & Hacar 2021) and assumed to originate from the higher density regions of molecular clouds. We also include the $(1, 1)$ NH_3 transition, another line thought to trace higher density gas than CO, and for which observational data are similarly plentiful (Ragan, Bergin & Wilner 2011; Ragan et al. 2012; Friesen et al. 2017; Fehér et al. 2022). The N_2H^+ and HCN intensities correspond to the $(1, 1, 2)$–$(0, 1, 0)$ and $(1, 0)$–$(0, 1)$ hyperfine components, respectively; other hyperfine components typically have intensities within a factor of a few of each other, so the exact choice of transition does not affect our conclusions.

At a density of $100\,\mathrm{cm^{-3}}$, all lines other than NH_3 are extremely weak ($< 10^{-5}$ K), but by $10^3\,\mathrm{cm^{-3}}$ the HCN, HCO^+, and CS lines have strengthened to $\sim 10^{-2}$ K and NH_3 is above 0.1 K. These intensities are well within reach of modern telescopes with a modest[6] investment of observing time. N_2H^+ remains several orders of magnitude fainter than this at $10^3\,\mathrm{cm^{-3}}$, and does not even begin to

approach comparable line brightnesses until a density of $10^4\,\mathrm{cm^{-3}}$. As noted above, this corresponds almost exactly to the density at which material appears to become gravitationally bound. By a quirk of its chemistry, and unlike any other molecular species we have investigated, N_2H^+ is only detectable in line emission in gas that will inevitably form stars.

4 DISCUSSION

The fact that N_2H^+ specifically traces gas that is in the process of forming stars, unlike most of the other species commonly used in this role, is due to its chemical behaviour. N_2H^+ reacts rapidly with CO to form HCO^+ and N_2, and due to the high abundance of CO at even moderate densities, this is typically the main route of destruction. The N_2H^+ abundance is therefore kept low until CO begins to deplete on to grain surfaces in significant quantities, which only begins to occur above a density of $10^4\,\mathrm{cm^{-3}}$ (Caselli et al. 2002; Tafalla et al. 2002, 2004; see also Priestley et al. 2023), and requires that the gas remains at or above this density for a significant period of time (Section 3.3). No equivalent reaction with CO exists for the other species, meaning that they exist in detectable quantities below what appears to be the star formation threshold, at least in the simulations presented here.

One implication of our results is that although molecules such as HCN and HCO^+ do trace the material that will eventually go on to form stars, they also trace gas that is only transiently shocked to moderately high density and so plays no part in the star formation process. This makes them unreliable as tracers of star-forming gas. At first glance, this seems incompatible with the tight correlation between HCN luminosity and the star formation rate (Gao & Solomon 2004; Neumann et al. 2023), which has been interpreted as HCN directly tracing the gas involved with star formation. However, the HCN $J = 1$–0 line intensity is known to be almost linearly correlated with the total column of gas (Tafalla, Usero & Hacar 2021), and therefore the mass. The correlation with star formation rate may therefore just be a correlation with the amount of molecular gas, rather than any specifically star-forming component of clouds. This would imply that the mass fraction of genuinely dense material is more or less constant, at least when averaged over large enough scales, which appears to be borne out by recent observational work (García-Rodríguez et al. 2023; Jiménez-Donaire et al. 2023).

On smaller scales, when the structure of individual molecular clouds can be resolved, the distinction between material traced by HCN and by N_2H^+ is likely to become important, as the ratio between their lines is clearly *not* constant (Pety et al. 2017; Tafalla, Usero & Hacar 2021). If HCN emission is assumed to trace star-forming gas, one might infer that the V14 model has a small but non-zero potential for star formation, despite the fact that it is actually in the process of dispersing. Tafalla, Usero & Hacar (2021) find a near-linear correlation between the strength of the N_2H^+ $J = 1$–0 line and the total column density of material when $N_H \gtrsim 3 \times 10^{22}\,\mathrm{cm^{-2}}$. We suggest that this can be used to estimate the mass of material

[6]Using the IRAM 30 m sensitivity calculator (https://oms.iram.fr/tse/), we estimate that a 3 mm line reaching an intensity of a few 10^{-2} K would be detectable (exceeding the sensitivity limit by a factor of a few) in $\lesssim 10\,\mathrm{h}$ of telescope time.

corresponding to the immediate reservoir for star formation, M_{SF}, via

$$M_{SF} = 310 \left(L_{N_2H^+} / \text{K km s}^{-1} \text{ pc}^2 \right) \text{ M}_\odot, \qquad (2)$$

where $L_{N_2H^+}$ is the luminosity of the N_2H^+ $J = 1$–0 line integrated over all hyperfine components, and the proportionality constant is converted from the column density–line intensity scaling factor $X_{N_2H^+} = 1.4 \times 10^{22} \text{ cm}^{-2} (\text{K km s}^{-1})^{-1}$ found by Tafalla, Usero & Hacar (2021). If this material is collapsing on approximately the freefall time for gas at a density of 10^4 cm^{-3}, $t_{ff} \sim 0.4 \text{ Myr}$, the star formation rate can be estimated as M_{SF}/t_{ff}, giving

$$SFR_{N_2H^+} = 775 \left(L_{N_2H^+} / \text{K km s}^{-1} \text{ pc}^2 \right) \text{ M}_\odot \text{ Myr}^{-1}. \qquad (3)$$

Based on the delay between the formation of dense gas and sink particles in Fig. 2, this quantity can be thought of as representing the expected star formation rate over the next ∼Myr of evolution, rather than an estimate of previous activity as provided by methods such as protostar counts.

Although our simulations do not include protostellar feedback, heating by newly formed protostars is expected to rapidly desorb molecules from grain surfaces in their vicinity (e.g. Viti et al. 2004), in particular CO. This increases the destruction rate of N_2H^+, and should eventually reduce its abundance back to undetectable levels. In reality, N_2H^+ and even its deuterated isotopologues are commonly detected towards regions of active star formation (Fontani et al. 2011; Friesen, Kirk & Shirley 2013; Cosentino et al. 2023), so its presence is not uniquely associated with material that is *about* to form stars, but also with material that already has. We do not consider this distinction hugely important: N_2H^+ still remains the best indicator of the potential for star formation of a molecular cloud, regardless of whether that potential has already been realized or not.

Finally, we note that our results are based on cloud properties, a radiation field, and an ionization rate appropriate for the solar neighbourhood, and may not apply in more extreme environments. Unlike most other observational studies (Kauffmann et al. 2017; Pety et al. 2017; Tafalla, Usero & Hacar 2021), Barnes et al. (2020) find that N_2H^+ behaves quite similarly to HCN in the W49 complex, a region of intense star formation activity. It is possible that an enhanced formation rate due to more highly ionized gas, or a reduced destruction rate due to greater photodissociation of CO, could change the chemical behaviour of N_2H^+ to something closer to that of HCN, making it more readily detectable at moderate densities. However, it also seems possible that these same effects would change the threshold density for star formation, so it is unclear what impact this would have on the properties of various molecules as tracers. While this is beyond the scope of this paper (the chemical network is only currently calibrated for solar neighbourhood conditions), we plan to investigate this topic more extensively in future work.

5 CONCLUSIONS

We have post-processed hydrodynamical simulations of molecular clouds with a full time-dependent chemical network, in order to investigate the ability of various molecular species to trace the reservoirs of material for star formation. We find that many molecules commonly used for this purpose, such as HCN and HCO⁺, exist in substantial quantities in gas that is presently at high density ($n_H \gtrsim 10^3 \text{ cm}^{-3}$), but only transiently, and that will eventually return to lower densities without undergoing any star formation. N_2H^+, by contrast, is only present in detectable amounts when the volume density of the gas exceeds 10^4 cm^{-3}, due to the onset of CO freeze-out. This coincides closely with the threshold density at which cloud material typically becomes gravitationally bound: the material traced by N_2H^+ will inevitably form stars (if it is not doing so already), unless disrupted by some outside process. Regions of clouds detected observationally in N_2H^+ therefore correspond directly to sites of current and future star formation, whereas other molecular tracers will give a misleading impression of a cloud's potential to form stars.

DATA AVAILABILITY

The data underlying this article will be shared on request.

REFERENCES

Anderson M. et al., 2021, MNRAS, 508, 2964
Barnes A. T. et al., 2020, MNRAS, 497, 1972
Bergin E. A., Tafalla M., 2007, ARA&A, 45, 339
Caselli P., Benson P. J., Myers P. C., Tafalla M., 2002, ApJ, 572, 238
Clark P. C., Glover S. C. O., 2014, MNRAS, 444, 2396
Clark P. C., Glover S. C. O., Klessen R. S., 2012, MNRAS, 420, 745
Clark P. C., Glover S. C. O., Ragan S. E., Duarte-Cabral A., 2019, MNRAS, 486, 4622
Cosentino G. et al., 2023, A&A, 675, A190
Enoch M. L., Evans N. J., II, Sargent A. I., Glenn J., Rosolowsky E., Myers P., 2008, ApJ, 684, 1240
Evans N. J., II, Kim K.-T., Wu J., Chao Z., Heyer M., Liu T., Nguyen-Lu'o'ng Q., Kauffmann J., 2020, ApJ, 894, 103
Fehér O. et al., 2022, ApJS, 258, 17
Fontani F. et al., 2011, A&A, 529, L7
Friesen R. K., Kirk H. M., Shirley Y. L., 2013, ApJ, 765, 59
Friesen R. K. et al., 2017, ApJ, 843, 63
Gao Y., Solomon P. M., 2004, ApJ, 606, 271
García-Rodríguez A. et al., 2023, A&A, 672, A96
Genel S., Vogelsberger M., Nelson D., Sijacki D., Springel V., Hernquist L., 2013, MNRAS, 435, 1426
Glover S. C. O., Clark P. C., 2012, MNRAS, 421, 116
Glover S. C. O., Mac Low M.-M., 2007, ApJS, 169, 239
Gong M., Ostriker E. C., Wolfire M. G., 2017, ApJ, 843, 38
Habing H. J., 1968, Bull. Astron. Inst. Neth., 19, 421
Holdship J., Viti S., Jiménez-Serra I., Makrymallis A., Priestley F., 2017, AJ, 154, 38

Hunter G. H., Clark P. C., Glover S. C. O., Klessen R. S., 2023, MNRAS, 519, 4152

Jenkins E. B., 2009, ApJ, 700, 1299

Jiménez-Donaire M. J. et al., 2023, A&A, 676, L11

Jones G. H., Clark P. C., Glover S. C. O., Hacar A., 2023, MNRAS, 520, 1005

Kaminsky A., Bonne L., Arzoumanian D., Coudé S., 2023, ApJ, 948, 109

Kauffmann J., Goldsmith P. F., Melnick G., Tolls V., Guzman A., Menten K. M., 2017, A&A, 605, L5

Klessen R. S., Glover S. C. O., 2016, in Revaz Y., Jablonka P., Teyssier R., Mayer L., eds, Star Formation in Galaxy Evolution: Connecting Numerical Models to Reality, Saas-Fee Advanced Course, Vol. 43. Springer-Verlag, Berlin, Heidelberg, p. 85

Könyves V. et al., 2015, A&A, 584, A91

Lada C. J., Lombardi M., Alves J. F., 2010, ApJ, 724, 687

Lee H.-H., Roueff E., Pineau des Forets G., Shalabiea O. M., Terzieva R., Herbst E., 1998, A&A, 334, 1047

McElroy D., Walsh C., Markwick A. J., Cordiner M. A., Smith K., Millar T. J., 2013, A&A, 550, A36

Neumann L. et al., 2023, MNRAS, 521, 3348

Pety J. et al., 2017, A&A, 599, A98

Priestley F. D., Clark P. C., Glover S. C. O., Ragan S. E., Fehér O., Prole L. R., Klessen R. S., 2023, MNRAS, 524, 5971

Prole L. R., Clark P. C., Klessen R. S., Glover S. C. O., 2022, MNRAS, 510, 4019

Ragan S. E., Bergin E. A., Wilner D., 2011, ApJ, 736, 163

Ragan S. E., Heitsch F., Bergin E. A., Wilner D., 2012, ApJ, 746, 174

Rawlings J. M. C., Hartquist T. W., Menten K. M., Williams D. A., 1992, MNRAS, 255, 471

Rigby A. J. et al., 2021, MNRAS, 502, 4576

Sembach K. R., Howk J. C., Ryans R. S. I., Keenan F. P., 2000, ApJ, 528, 310

Springel V., 2010, MNRAS, 401, 791

Tafalla M., Myers P. C., Caselli P., Walmsley C. M., Comito C., 2002, ApJ, 569, 815

Tafalla M., Myers P. C., Caselli P., Walmsley C. M., 2004, A&A, 416, 191

Tafalla M., Usero A., Hacar A., 2021, A&A, 646, A97

Tress R. G., Smith R. J., Sormani M. C., Glover S. C. O., Klessen R. S., Mac Low M.-M., Clark P. C., 2020, MNRAS, 492, 2973

Tritsis A., Bouzelou F., Skalidis R., Tassis K., Enßlin T., Edenhofer G., 2022, MNRAS, 514, 3593

van der Tak F. F. S., Black J. H., Schöier F. L., Jansen D. J., van Dishoeck E. F., 2007, A&A, 468, 627

Viti S., Collings M. P., Dever J. W., McCoustra M. R. S., Williams D. A., 2004, MNRAS, 354, 1141

This paper has been typeset from a T_EX/L^AT_EX file prepared by the author.